PHOTONICS Research

Experimental study of neuromorphic node based on a multiwaveband emitting two-section quantum dot laser

George Sarantoglou,[1,3] Menelaos Skontranis,[1] Adonis Bogris,[2] and Charis Mesaritakis[1,*]

[1]Department of Information and Communication Systems Engineering, University of the Aegean, Palama 2, Karlovassi 83200 Samos, Greece
[2]Department of Informatics and Computer Engineering, University of West Attica, Aghiou Spiridonos, 12243 Egaleo, Athens, Greece
[3]e-mail: gsarantoglou@aegean.gr
*Corresponding author: cmesar@aegean.gr

Received 27 October 2020; revised 18 January 2021; accepted 25 January 2021; posted 25 January 2021 (Doc. ID 413371); published 16 March 2021

In this work, we present experimental results concerning excitability in a multiband emitting quantum-dot-based photonic neuron. The experimental investigation revealed that the same two-section quantum dot laser can be tuned through a simple bias adjustment to operate either as a leaky integrate and fire or as a resonate and fire neuron. Furthermore, by exploiting the inherent multiband emission of quantum-dot devices revealed by the existence of multiple lasing thresholds, a significant enhancement in the neurocomputational capabilities, such as spiking duration and firing rate, is observed. Spike firing rate increased by an order of magnitude that leads to an enhancement in processing speed and, more importantly, neural spike duration was suppressed to the picosecond scale, which corresponds to a significant temporal resolution enhancement. These new regimes of operation, when combined with thermal insensitivity, silicon cointegration capability, and the fact that these multiband mechanisms are also present in miniaturized quantum-dot devices, render these neuromorphic nodes a proliferating platform for large-scale photonic spiking neural networks.

https://doi.org/10.1364/PRJ.413371

1. INTRODUCTION

Bio-inspired computing has emerged in the last five years as a promising candidate to tackle the inefficiency of conventional von Neumann architectures to address machine-learning related problems [1]. More specifically, the vision of dedicated hardware that mimics the principle of operation of biological neural circuits is extremely appealing performance- and energy-consumption-wise. Having in mind these two aspects, photonic technology offers a proliferating platform for the development of such systems due to advantages such as low loss, inherent parallelism through wavelength-time multiplexing, ultralow response time, and similarity of dynamics with biological neurons [1]. Semiconductor lasers are active photonic components that fit really well in the neuromorphic landscape because they possess all the aforementioned advantages. In previous works, laser neurons have been examined both theoretically and experimentally utilizing different schemes, namely, coherent/noncoherent optical injection [2–4], optical feedback [5], two-section lasers [gain and saturable absorber (SA)] [6–8], microdisk lasers [9], 2D photonic crystals [10], and polarization-switching vertical cavity surface emitting lasers (VCSELs) [11].

With respect to photonic-based solutions, quantum dot (QD) lasers in particular, can be utilized as extremely efficient neuromorphic nodes, since they present multiple benefits compared to traditional quantum well (QW) devices, such as temperature insensitivity and stability [12–14]. These aspects are of utmost importance for successful large-scale integration of laser-based spiking neural networks. Additionally, QDs can make silicon-based lasers possible [15], paving the way to seamless integration with other silicon photonic neuromorphic architectures [16]. In the literature, single-section QD laser neurons in optical injection schemes have been studied both theoretically and experimentally [17–19]. Moreover, we have recently provided experimental evidence of neuromorphic operation from a QD two-section device, at the same time achieving all-optical isomorphism to excitatory and inhibitory neurons [20].

In order to harness the full potential of biological neural motifs, it is important to develop photonic components able to replicate the neurocomputational characteristics of biological neurons. A detailed picture of the most important neurocomputational properties is presented in Table 1 [21]. The most commonly encountered neurons are Class I integrators and resonators. These two types of neurons differ in terms of the existence of fast subthreshold small amplitude oscillations that can be unmasked by the presence of noise. In particular, integrators reveal no subthreshold oscillations because they are highly dumped systems, while resonators do reveal such oscillations. The other neuronal differences that exist between these two categories stem from this basic difference [21]. In particular, integrators reveal an adjustable firing rate depending on the input strength (rate encoding scheme). Moreover, they present a well-defined neural threshold, which means that when the external triggering is below a certain value, no spikes are observed, whereas beyond that threshold, spike events of relatively constant amplitude are generated (all-or-none spiking). On the other hand, in resonators, the firing rate is limited in a small frequency range that is dictated by the subthreshold oscillations. In general, they do not exhibit a well-defined threshold value, but a threshold area. When the energy of external triggering is within a certain energy area, spike events can be produced whose amplitude is variable, depending on the strength of the applied triggering [21]. This results in the absence of all-or-nothing spiking, which in experiments can be observed through spike events whose amplitude presents large standard deviation due to the presence of noise-induced triggering. An important exception is the case of slow-fast systems, where the threshold area is so thin that it resembles a well-defined threshold known as the quasi-threshold [22]. In this case, the transition from resting to spiking dynamics is known as a Canard explosion [23], a situation that has been observed in optically injected lasers [18,24] and photonic crystals [10]. Last but not least, resonators present frequency preference, which means that firing efficiency is enhanced when the frequency of the input signal matches the subthreshold oscillation frequency.

Application-wise, the integrators are important as processing units that are capable of encoding information in the time signature of various all-or-none spike events. Resonators, due to their frequency selectivity, can act as bandpass filters that transform the input signal in a spike train. Moreover, they can be used to achieve selective communication between different neural groups [25]. These two types of neurons can be efficiently transferred in the photonic domain, through QD devices, due to the aforementioned pivotal advantages that they process. Up to now, QDs have been exploited so as to realize integrator dynamics in a two-section laser configuration [20] and through optical injection-based triggering [17]. With respect to resonators, the state of the art in QDs consists of an optically injected, edge-emitting, single-section laser, with emitting only from the ground-state (GS) waveband. This device allows the recording of microsecond spikes whose origin could be traced to intracavity thermal effects [18]. Thus, this implementation exhibits limited temporal resolution compared to conventional QW-based resonators [26]. This reduction in temporal resolution (spike duration) can greatly impact the accuracy of bio-inspired learning techniques such as spike-dependent plasticity [27], as well as the accuracy of the various spike encoding schemes [28].

In this work, our goal is to further advance the concept of two-section QD neurons introduced in our previous work [20]. Compared to Ref. [20], we provide an in-depth analysis of the excitatory QD neuron, which is the most common in neural networks, and present its manifestation under various laser bias conditions. In particular, we present evidence that the two-section QD laser operates as an integrator by exploiting the thermo-optic coupling, whereas the Q-switching effect that is strongly related to the multiwaveband-related dynamics is linked to resonate and fire operation. Moreover, the study of different bias regimes reveals for the first time the impact of multiwaveband emission, not on the neuron's type (excitatory/inhibitory) as it was shown in Ref. [20], but on its performance. The existence of multiwaveband dynamics allowed for spike events of subnanosecond temporal width, thus leading to highly improved temporal resolution and, additionally, to an increase of the firing rate by 1 order of magnitude. This improvement is more important, when considering the fact that the devices used in this work have an increased footprint and achieve performance similar to miniaturized lasers. Taking into consideration that the multiband behavior exploited here is also present in small footprint QD structures, this work paves new exploration paths for QD neurons. Furthermore, since a two-section device can be triggered both electro-optically through current modulation [29] and all-optically by applying external optical injection [30], we employ a twofold approach; on one hand we use the solitary laser neuron's injection current as a neural triggering mechanism, which is the simplest way to determine its neurocomputational properties [30]. Then we demonstrate an all-optical, application-focused scenario and analyze the effect of multiwaveband emission in the temporal resolution by triggering the laser with mode-locked pulses from a master QD laser. This twofold investigation signifies that

Table 1. Major Neurocomputational Properties [21]

Properties	Integrators		Resonators	
Excitability	Class I	Class II	Class II	
Subthreshold oscillations	No		Yes	
Frequency preference	No		Yes	
Threshold	Well defined		May not be defined	
All-or-none spiking	Yes		No (*yes)	
Bistability	No	Yes	No	Yes
Bifurcation	Saddle node on limit cycle	Saddle node off limit cycle	Supercritical Hopf (*canard explosion)	Subcritical Hopf

the proposed scheme can provide excitability through both electro-optic and all-optical triggering.

2. EXPERIMENTAL SETUP

The full-scale experimental setup, illustrated in Fig. 1, consists of two InAs/InGaAs Fabry–Perot, edge emitting, two-section QD lasers, connected in a master laser (ML)/slave laser (SL) configuration. The ML acts as the external stimulus by operating in a GS passive mode–locking regime, emitting pulses with a temporal width of <10 ps. The active material consists of 10 QD layers into a 440 nm GaAs waveguide surrounded by an $Al_{35\%}Ga_{65\%}As$ layer, whereas the cavity length is 4 mm. The SL acts as a photonic neuron. Its cavity length is 2 mm, and it consists of five QD layers. The gain/SA ratio is 0.85/0.15 for both lasers. The temperature is controlled by a Peltier element in a closed control loop. The temperatures are set to 33°C for the ML and 20°C for the SL. This temperature variation is set so their optical spectra partially overlap, despite the slightly different emission wavelengths of each structure.

At first, we study only the behavior of the SL under injection current variations; thus only a part of the aforementioned setup is used (Part I in Fig. 1), while later the full-scale unidirectional optical injection setup is exploited (Part II in Fig. 1). A variable optical attenuator (VOA) is used to control the optical power injected in the SL. A photodiode with 6 GHz bandwidth, followed by a real-time oscilloscope with 40 GSample/s data acquisition capability is used to track the optical output of the SL, and an optical spectrum analyzer (OSA) with 0.05 nm resolution is used to measure the optical spectrum at both bands.

3. EXPERIMENTAL INVESTIGATION OF MULTIPLE GS THRESHOLDS

Excitability in a conventional two-section laser is achieved by biasing it below its lasing threshold and applying an external stimulus [30]. In this case, the SA acts as a thresholder, determining the necessary strength of the input signal so as to trigger an optical spike [20]. In the case of QD-based lasers, the multiwaveband emission capabilities, namely, GS/excited state

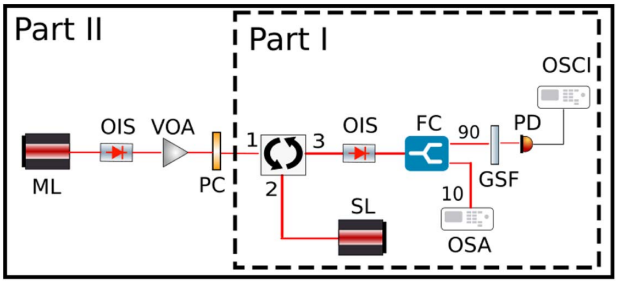

Fig. 1. Experimental setup. ML, master laser; SL, slave laser; VOA, variable optical attenuator; PC, polarization controller; OC, optical circulator; FC, fiber coupler; OSA, optical spectrum analyzer; GSF, ground-state passband filter; PD, photodiode; and OSCI, oscilloscope. The dashed box contains the first experiment (Part I), which was based on the electro-optic triggering of the SL through current injection, whereas the full line box contains the full unidirectional optical injection setup (Part II).

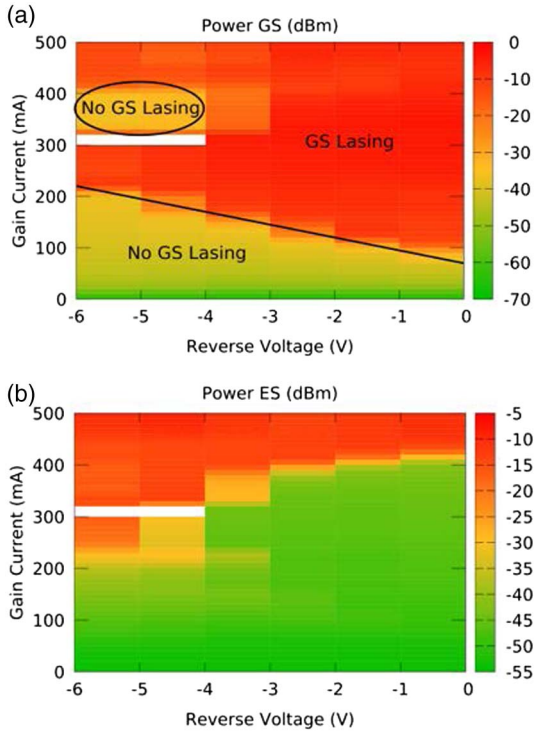

Fig. 2. (a) GS optical power of the QD SL, for various gain current and SA reverse voltage bias conditions; (b) ES optical power of the QD SL, for various gain current and SA reverse voltage bias conditions. The white regions refer to corrupt measurements, which, however, correspond to bias regimes that are not related to the neurocomputational properties of the SL.

(GS/ES) emission, allow multiple subthreshold regimes where emission occurs from a single waveband, while the other one is set below its lasing threshold. This behavior can affect the laser's dynamics and modify the anticipated excitable operation and performance. In this work, we focus on operational regimes where GS emission is below the threshold, while ES emission can be on or off. In this scope, in Fig. 2 the optical power for the GS [Fig. 2(a)] and ES band [Fig. 2(b)] of the solitary SL as a function of the applied gain current and reverse voltage at the SA is presented.

The lasing threshold of GS emission increases with the increase of reverse voltage due to the increase of the SA's unsaturated losses [31]. Moreover, GS lasing appears to have two discrete thresholds for reverse voltages above 4 V. The first is observed for low current injection (≈200 mA) and the second one for higher current injection (≈400 mA), associated with ES lasing [compare Figs. 2(a) and 2(b)]. In order to shed light on the origin of the two discrete GS thresholds, in Figs. 3(a) and 3(b), the GS and ES optical spectra are demonstrated versus injection current for 5 V reverse voltage. For low injection current, GS and ES lasing is achieved simultaneously due to the small cavity length and the low number of QD layers (first GS lasing threshold) [32,33]. As injection current increases, GS lasing is suppressed due to the GS quenching effect [34]. After this point, higher injection current leads to ES spectral splitting, where two discrete sets of longitudinal modes are

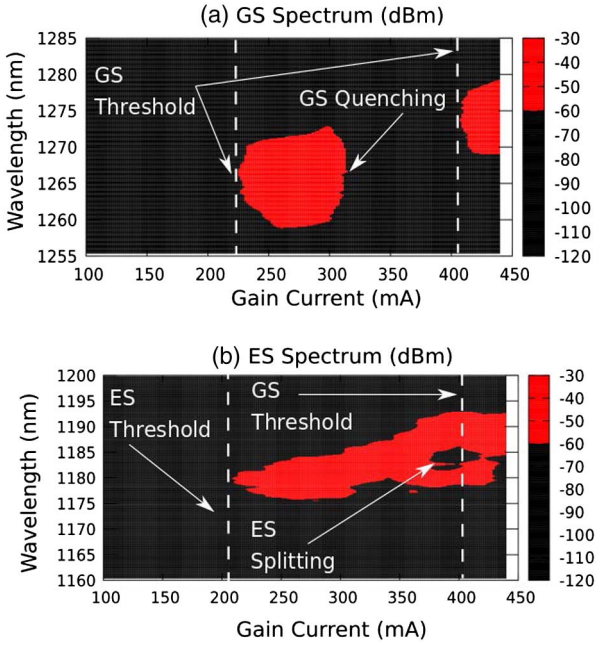

Fig. 3. Development of (a) GS and (b) ES spectrum with gain current for $V_{rev} = 5\,V$.

lasing. The spectral separation ($\Delta\lambda$) between the centers of each set of modes increases with current and can extend up to $\Delta\lambda = 9.5\,nm$ for 400 mA. When injection current increases beyond 400 mA, $\Delta\lambda$ starts being reduced, and GS is forced again above the threshold (second GS threshold). For higher current injection (440 mA), ES splitting completely vanishes. This behavior is observed here for the first time and is probably linked to gain suppression mechanisms similar to those responsible for GS spectral splitting [35].

This spectral evolution can provide an insight into the dynamics responsible for the "second" GS threshold. In particular, ES splitting is linked to gain suppression effects like spectral hole burning at the central longitudinal modes [35,36]. Therefore, this gain suppression reduces the stimulated emission process at the ES, allowing the reaccumulation of free carriers at the GS, and subsequently evoking GS lasing. When GS lasing is triggered, GS free carriers are depleted, and the flow of carriers in the ES is reduced. This effect, in turn, reduces the gain in the ES and gradually terminates the saturation-induced splitting effect (see Fig. 3).

The key feature is that the carrier dynamics at each band in this new regime are inherently different compared to the conventional single-band threshold of devices. Thus, in the following paragraphs, we focus on analyzing the excitability for these two regimes, which involve subthreshold GS biasing.

4. EXPERIMENTAL INVESTIGATION OF EXCITABILITY REGIMES USING INJECTION CURRENT

The neurocomputational properties of an excitable system can be deduced by performing a bifurcation analysis (see Table 1) [21]. In particular, in excitable systems, the variation of a single parameter known as the bifurcation parameter leads to the transition from a resting state to oscillatory dynamics. In two-section devices, the simplest way to study the excitability-related bifurcation is the variation of the current injection close to the laser threshold [30].

A. Neurocomputational Properties Close to the Low (First) GS Current Threshold

For reverse voltage $V_{rev} \le 4\,V$, only the low-injection GS threshold exists. For $V_{rev} = 4\,V$, the transition from resting dynamics to self-pulsations is characterized by microsecond all-or-none spikes with very low repetition frequency [Fig. 4(a)], whose origin is related to the optothermal coupling effect [37,38]. Unlike single-section QD devices [38], no fast small-amplitude oscillations are observed at the resting state, which indicates that the SL behaves as an integrator. The firing rate increases with gain current rate encoding [Fig. 4(b)] as in Class I integrator systems (Table 1). This behavior may be linked to a homoclinic saddle node bifurcation, which was observed recently in single-section QD lasers [39]. It is important to note that this dynamic regime can be traced for all $V_{rev} \le 4\,V$.

On the other hand, for $V_{rev} = 5\,V$ and gain current close to 218 mA, although the laser is set below/near its threshold, perturbations that evoke a radical shift in the laser's behavior are observed. In Fig. 3, it can be seen that for this bias regime GS/ES emission thresholds coincide, meaning that the GS dynamics are also affected by the ES band. Although the power of ES is weak in this case, as shown in Fig. 2, its dynamics still affect the GS waveband through the scattering rates as opposed to the case of 4.5 V, where the influence of the ES waveband becomes significant—close to 350 mA. The temporal width of the generated spikes is considerably reduced, from the microsecond to the nanosecond scale. This indicates that these pulsations are linked to Q-switching effects [29], which in turn are possibly linked to GS/ES interplay [40]. The mean amplitude and standard deviation of the spikes recorded at the photodiode are depicted in Fig. 5 as a function of the gain current. The low standard deviation indicates the property of all-or-none spiking.

In Fig. 6, the RF spectrum and time traces for 218 mA (a), 219 mA (b), and 221 mA (c) are presented. For 218 mA, the laser is below its threshold, and no spikes are recorded, but in the RF spectrum, a clear peak at 17.2 MHz is evident, corresponding to subthreshold pulsations unmasked by noise [21]. For 219 mA, the resting state coexists with noise-triggered spike

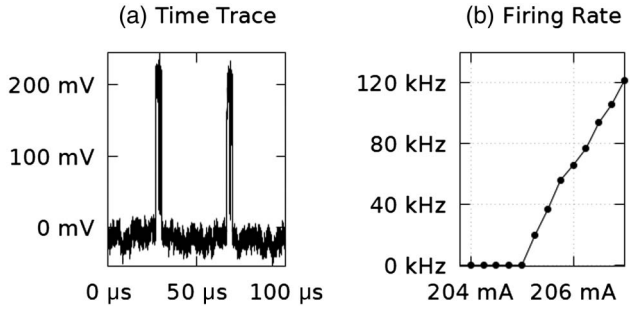

Fig. 4. (a) Two opto-thermal spike events for $V_{rev} = 4\,V$ and $I_{bias} = 205.25\,mA$; (b) firing rate of the generated spike events as a function of the gain current for the same reverse voltage bias.

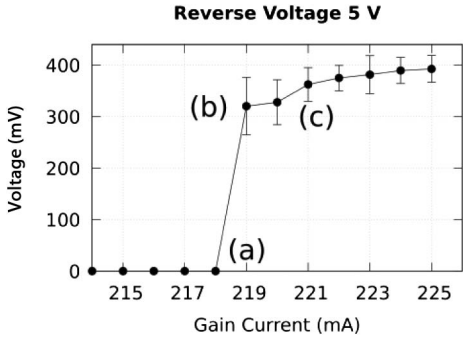

Fig. 5. Spike amplitude for $V_{rev} = 5\,V$ close to the low GS injection threshold. The points (a), (b), and (c) correspond to $I_{bias} = 218$, 219, and 221 mA.

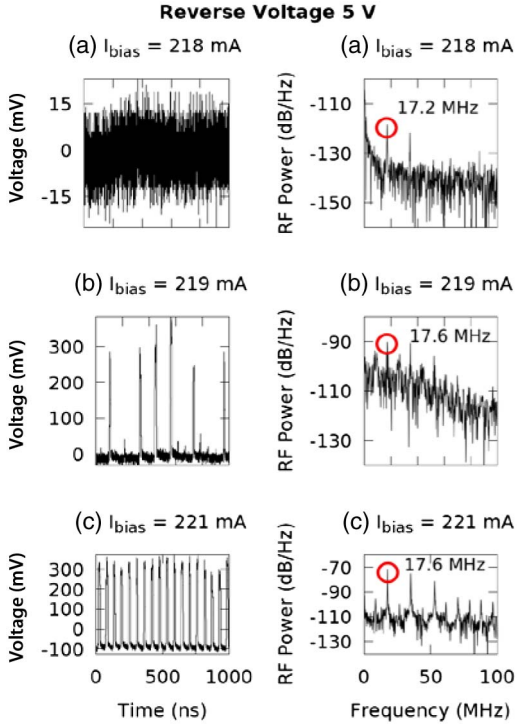

Fig. 6. RF spectra and time traces for 5 V reverse voltage and $I_{bias} = 218$ (a), 219 (b), and 221 mA (c).

events. Interestingly, these spikes are built upon the 17.6 MHz subthreshold oscillations, as the RF spectrum reveals. By further increasing the gain current to 221 mA, the laser fully enters the Q-switching regime, and the RF spectrum exhibits again a peak at 17.6 MHz. This behavior is associated with a Hopf bifurcation [41], and consequently, the SL when biased below 218 mA acts as a resonator [21]. The Hopf bifurcation is common in two-section lasers when the SA saturates more easily and at the same time recovers much faster than the gain section [42,43], which in our case can be explained by the small SA-to-gain ratio and the ultrafast dynamics of the QD SA [44]. For $V_{rev} = 5.5, 6\,V$ and low injection current, similar qualitative and quantitative results are observed. The small standard deviation of the spike amplitude, along with the existence of subthreshold oscillations that dictate the spiking frequency, leads to the conclusion that the transition from resting to spiking dynamics is due to a canard explosion, and the system presents a quasi-threshold. This situation has been shown numerically for two-section schemes in Ref. [45].

B. Neurocomputational Properties Close to the High (Second) GS Current Threshold

As stated above, for $V_{rev} \geq 4.5$ V, the SL reveals an additional high-injection GS threshold, along with stable ES emission. For $V_{rev} = 5\,V$ and $I_{bias} \approx 410\,mA$, the evolution of spike amplitude with the current is shown in Fig. 7. The mean amplitude is close to the case of the low GS threshold, but the standard deviation has increased significantly. For instance, at 412 mA, spike events with amplitude from 0.12 to 0.28 V have been observed, indicating the loss of all-or-nothing dynamics. The RF spectrum at 411 mA reveals a peak at 150 MHz, whose power increases with the gain current (Fig. 7). The dynamical transition is again via a Hopf bifurcation, and the SL below 411 mA acts as a resonator. The same qualitative and quantitative behavior is observed for $V_{rev} = 4.5, 5.5, 6\,V$, and the proper injection current so as to bias the laser at the "second" GS threshold.

The loss of all-or-nothing dynamics can be linked to the increase of ES emission for higher gain current injection. In particular, the increase of ES photogenerated carriers due to the increased ES emission in the SA can lead to the relaxation of ES carriers to the GS level (the photopumping effect) [46]. Consequently, the GS level of the SA saturates more easily for increased ES emission, and the transition of the peak amplitude with gain current is less abrupt [45]. This slower transition in Hopf bifurcation is associated in neurons with the broadening of the neural threshold area, and consequently, the absence of all-or-nothing dynamics [21].

It is important to notice the increase of the firing rate by 1 order of magnitude (150 MHz compared to 17.6 MHz) in the case of the second GS threshold. Based on the fact that GS–ES interplay can lead to strong Q-switching pulsations at multigigahertz frequencies [47] at the onset of dual GS–ES lasing, even for long laser devices, this second GS threshold

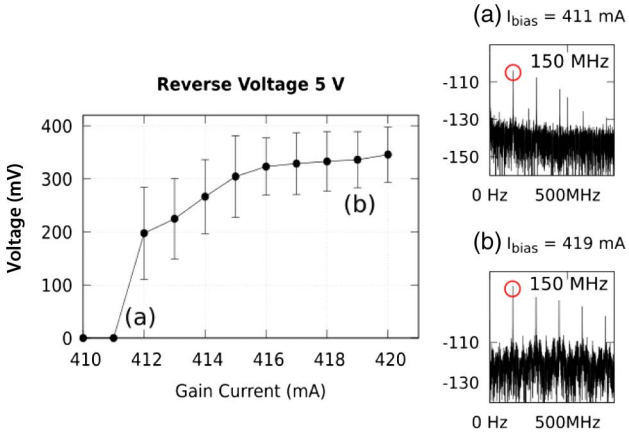

Fig. 7. Mean amplitude and standard deviation of the GS spike events for biasing close to the high GS threshold and $V_{rev} = 5$ V. The marks (a) and (b) correspond to $I_{bias} = 411$ and 419 mA.

can potentially unlock neurons with an increased firing rate. This can result in enhanced processing speed and at the same time, adequate optical power for neural network scaling.

5. RESONATE AND FIRE NEURAL OPERATION USING OPTICAL INJECTION FROM A MASTER QD LASER

A. Optical Excitation with Mode-Locked Pulses

The above analysis revealed the bias conditions under which the QD neuron can act as an integrator or resonator. Nonetheless, an electro-optical-driven laser neuron is of little interest, since the generated neural network is again subject to all the limitations of RF circuits. Therefore, it is vital to provide evidence of all-optical excitability. To this end, the setup is equipped with an ML that provides optical stimuli in the form of picosecond duration mode-locked GS pulses. The ML is biased at 3 V reverse voltage, whereas the gain current can affect simultaneously two experimental parameters: the optical power of the ML pulses and the frequency detuning between the ML and SL. The change of the frequency detuning is caused by the redshift of the ML GS spectrum with increased gain current, as is illustrated in Fig. 8(a) for 320 and 440 mA biasing of the ML. In the same figure, the ML spectrum is compared with the GS spectrum from the SL when it is biased at 4.5 V and 417 mA. The range where the ML current was varied (360–450 mA) did not result in a noticeable power variation, probably due to gain saturation, whereas minor variations were compensated through a polarization controller. It is clear that the low free spectral range of the lasers compared to the resolution of the OSA ($\Delta\lambda = 0.05$ nm) and the asymmetric, wideband emission due to the inhomogeneous broadening hinder the definition of a typical ML–SL detuning. Based on this, in Fig. 8(b), it is shown that the optical detuning between the SL–ML's longitudinal modes caused by varying ML current determines the efficiency of the optical injection; this effect is traced through computing the number of spikes triggered at the SL. The SL in this case is biased at 4.5 V. The normalized number of spikes in Fig. 8(b) is calculated by counting the number of spikes in a predefined time window of 50 μs duration for all cases. Then the results are normalized with respect to the maximum number of spikes that are observed close to 450 mA. It must be noted that the free spectral range of our Fabry–Perot devices has a resolution below the resolution of the OSA, while the inhomogeneous broadening of the QDs provides a highly asymmetric wideband spectrum, exhibiting multiple peaks [see Fig. 8(a)]. For these reasons, the exact detuning between the ML and the SL could not be computed, and thus the optical injection efficiency is illustrated in terms of the ML gain current in Fig. 8(b).

In Fig. 9, the mean amplitude of spikes as a function of the incoming optical strength is presented when the SL is biased at $V_{rev} = 5$ V and either at $I_{bias} = 218$ mA (first GS threshold) or $I_{bias} = 409$ mA (second GS threshold). Contrary to Fig. 8, where the SL is biased at 4.5 V, in the case of 5 V, the ML achieves the optimum triggering efficiency for ML gain current equal to 400 mA, both in the case where the SL is biased close to its low and high GS thresholds. For 218 mA, the optical injection threshold is observed at −12 dBm, whereas for 409 mA it is observed at −23 dBm. Comparing these two figures, the loss of all-or-nothing threshold is once again observed in the case of the high current biasing.

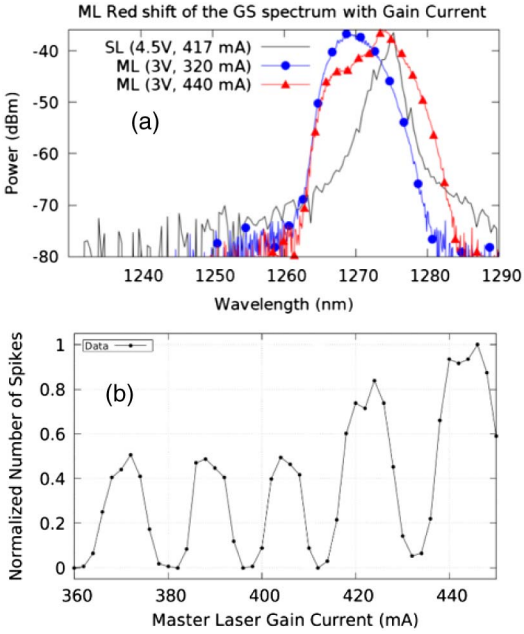

Fig. 8. (a) Detuning between the SL spectrum (black solid line) and the ML spectrum changes with increasing ML gain current (320 mA for the blue line with circles and 480 mA for the red line with triangles); (b) dependence of the number of generated spike events on the ML gain current. The SL is biased at $V_{rev} = 4.5$ V and $I_{bias} = 406$ mA, whereas the ML is biased at $V_{rev} = 3$ V.

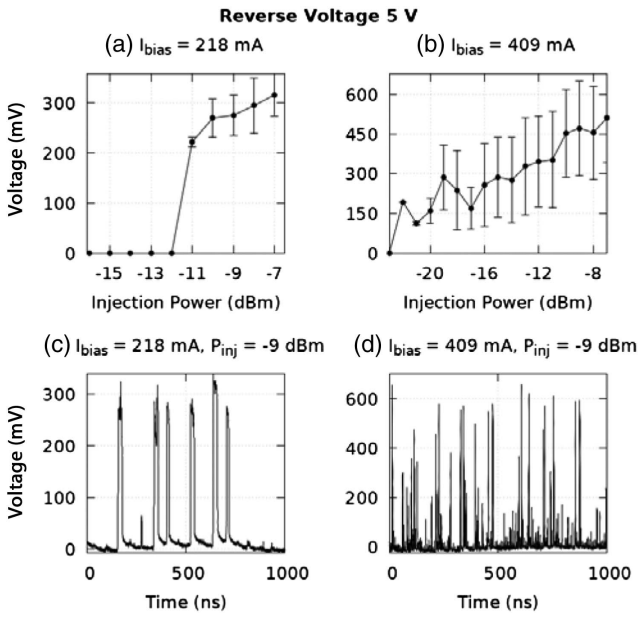

Fig. 9. Mean amplitude and standard deviation of GS spike events as a function of the injection strength for optical triggering, with the ML biased at 3 V reverse voltage. SL is biased at 5 V reverse voltage and (a) 218 mA—close to the low gain current threshold; (b) 409 mA—close to the high gain current threshold. Time traces for mean injection power equal to −9 dBm are shown for (c) 218 mA and (d) 409 mA.

In Figs. 9(c) and 9(d), time traces are illustrated corresponding to injection strength equal to –9 dBm. For $I_{bias} = 218$ mA [Fig. 9(c)], the spike events are all-or-nothing, whereas for $I_{bias} = 409$ mA [Fig. 9(d)] it can be seen that all-or-nothing excitability is lost. Moreover, the number of generated spike events is lower in the case of 218 mA as compared to the case of 409 mA, due to the higher firing rate in the second case, as was shown by the RF diagrams.

B. Multiwaveband Assisted Enhancement of the Temporal Resolution

Another key observation is the variation of the spike's duration versus the existence of ES emission and the reverse bias [48]. In Fig. 10(a), the SL is biased below its low GS current threshold and is triggered by the ML for various reverse bias conditions. At 4.5 V, mean full width at half-maximum (FWHM) is equal to 604 ns, corresponding to optothermal pulsations. Increasing the reverse voltage to 5 V causes the transition from optothermal excitation to Q-switching-based excitation, which results in a reduction of the mean FWHM by 2 orders of magnitude, to 19 ns. This change can be attributed to the strong interplay between GS and ES wavebands, as is discussed in Section 4.A. Each subsequent 0.5 V decrease results in a reduction of the mean FWHM by 1 order of magnitude, namely, 2.5 ns for 5.5 V and 0.86 ns for 6 V. The steep reduction with increased voltage may be related not only to the faster carrier escape dynamics in the SA [44], but also to the increased ES emission due to higher unsaturated losses [31].

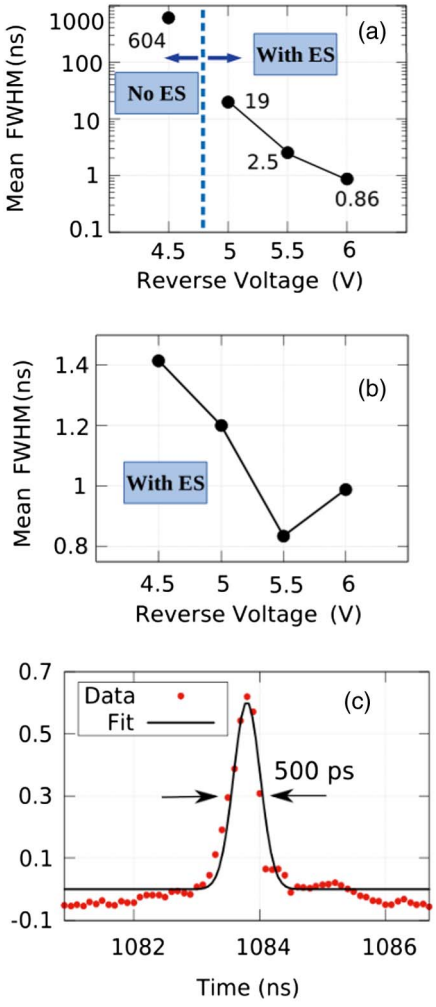

Fig. 10. Spike width as a function of the reverse bias and ES emission (a) close to the low GS current threshold; (b) close to the high GS current threshold. (c) 500 ps spike event recorded for SL with $I_{bias} = 407$ mA and $V_{rev} = 5.5$ V.

To shed light on the contribution of ES emission, we reproduce the experiment, but this time, the SL is biased close to the high GS gain threshold, where ES emission is increased [Fig. 10(b)]. The mean FWHM is in the nanosecond scale, even for $V_{rev} = 4.5$ V, and weakly varies for increasing reverse voltage. This outcome indicates the significant contribution of ES emission to the temporal resolution. In Fig. 10(c), a 500 ps spike event is illustrated for 5.5 V biasing, which is remarkably close to the 200 ps temporal width provided by the two-section QW-based microlaser [6]. Since the reduction of the cavity size is linked to shorter Q-switched pulses [49] and a lower ES threshold [31], we expect that the further reduction of cavity size will lead to important improvements regarding the temporal resolution.

6. DISCUSSION

The aforementioned results showcase that the two-section QD laser is able to accomplish both integrate and fire and resonate and fire dynamics, whereas its performance can be enhanced by exploiting the GS–ES interplay. However, the recorded results render the 2 mm long edge-emitting laser adequate only as a proof-of-principle, due to its high energy consumption and the low firing rate achieved compared to other laser-neuron approaches [1], which accomplish a threshold current condition of a few milliamperes and firing rates in the multigigahertz regime. The striking difference between our device and the laser-neurons in the literature can mainly be attributed to the significantly smaller cavity size of the latter (VCSEL devices [7], micropillars [6]).

The main goal of this work is to provide a proof of concept about the new neurocomputational regimes of QD lasers and pave the way for the exploration of these devices as artificial neurons. This fact is enhanced by the fact that the multiwaveband dynamics that are investigated in this work can be transferred to smaller-scale devices, where, in fact, they will be enhanced due to the increased unsaturated losses [32]. Thus, it is anticipated that the design of small-cavity QD lasers (i.e., VCSELs) will provide superior performance as cognitive processors by achieving an extremely low lasing threshold condition due to their 3D confinement structure [50], as well as multigigahertz repetition frequencies [51]. These small-scale devices will still benefit from the thermal stability and the improvements associated with the multiwaveband dynamics that were presented in this and our previous work [20]. These QD-based devices will be able to operate as truly energy-efficient, versatile, and silicon-compatible neuromorphic nodes.

7. CONCLUSION

QD lasers, although rarely investigated as potential photonic neural components, have begun attracting notable attention recently due to their thermal insensitivity and their capability of offering seamless integration with silicon photonic platforms.

Within this scope, in this work we performed an experimental investigation of the excitable regimes of a multisection QD laser, using injection current in a solitary laser, and optical injection in a unidirectional ML–SL configuration. The multisection devices are preferred due to the reduced complexity compared to other optical schemes for implementing large-scale neural networks. Results confirm that QD semiconductor lasers can be biased to operate as integrators exploiting the thermo-optic coupling effect, while for higher reverse voltage and in the presence of multiband emission (ES lasing), lasers are driven in a resonate and fire regime. Moreover, a new multi-GS threshold is observed for the first time, originating from the multiwaveband dynamics (GS quenching, ES splitting). The existence of two discrete GS current thresholds is used to demonstrate the significant contribution of the ES emission to the optimization of the temporal resolution. We expect that an increase of ES emission associated with smaller QD devices will further boost these improvements. Consequently, these results, combined with our previous work [20], where the QD laser was studied in terms of its inhibitory and excitatory dynamics, show that the multi-section QD lasers constitute highly flexible devices able to unlock a rich palette of neural attributes such as resonate and fire dynamics, integrate and fire dynamics, along with all-optical excitatory and inhibitory triggering. These properties, which are explicitly related to QDs, when transferred in small-scale devices that benefit from low power consumption, higher temporal resolution, and multigigahertz repetition frequency, will pave the way to the development of truly efficient all-optical spiking neural networks.

Funding. Hellenic Foundation for Research and Innovation; General Secretariat for Research and Technology (2247 NEBULA Project).

Acknowledgment. The authors would like to thank the members of the photonic technology laboratory in the Department of Informatics and Telecommunications at the University of Athens for hosting the experimental activities of the NEBULA project.

Disclosures. The authors declare no conflicts of interest.

REFERENCES

1. P. R. Prucnal and B. J. Shastri, *Neuromorphic Photonics* (CRC Press, 2017).
2. S. Barland, O. Piro, M. Giudici, J. R. Tredicce, and S. Balle, "Experimental evidence of van der Pol–Fitzhugh–Nagumo dynamics in semiconductor optical amplifiers," Phys. Rev. E **68**, 036209 (2003).
3. M. Turconi, B. Garbin, M. Feyereisen, M. Giudici, and S. Barland, "Control of excitable pulses in an injection-locked semiconductor laser," Phys. Rev. E **88**, 022923 (2013).
4. B. Garbin, D. Goulding, S. P. Hegarty, G. Huyet, B. Kelleher, and S. Barland, "Incoherent optical triggering of excitable pulses in an injection-locked semiconductor laser," Opt. Lett. **39**, 1254–1257 (2014).
5. H. J. Wünsche, O. Brox, M. Radziunas, and F. Henneberger, "Excitability of a semiconductor laser by a two-mode homoclinic bifurcation," Phys. Rev. Lett. **88**, 023901 (2001).
6. F. Selmi, R. Braive, G. Beaudoin, I. Sagnes, R. Kuszelewicz, and S. Barbay, "Relative refractory period in an excitable semiconductor laser," Phys. Rev. Lett. **112**, 183902 (2014).
7. M. A. Nahmias, B. J. Shastri, A. N. Tait, and P. R. Prucnal, "A leaky integrate-and-fire laser neuron for ultrafast cognitive computing," IEEE J. Sel. Top. Quantum Electron. **19**, 1800212 (2013).
8. F. Selmi, R. Braive, G. Beaudoin, I. Sagnes, R. Kuszelewicz, and S. Barbay, "Temporal summation in a neuromimetic micropillar laser," Opt. Lett. **40**, 5690–5693 (2015).
9. K. Alexander, T. Van Vaerenbergh, M. Fiers, P. Mechet, J. Dambre, and P. Bienstman, "Excitability in optically injected microdisk lasers with phase controlled excitatory and inhibitory response," Opt. Express **21**, 26182–26191 (2013).
10. A. M. Yacomotti, P. Monnier, F. Raineri, B. B. Bakir, C. Seassal, R. Raj, and J. A. Levenson, "Fast thermo-optical excitability in a two-dimensional photonic crystal," Phys. Rev. Lett. **97**, 143904 (2006).
11. A. Hurtado and J. Javaloyes, "Controllable spiking patterns in long-wavelength vertical cavity surface emitting lasers for neuromorphic photonics systems," Appl. Phys. Lett. **107**, 241103 (2015).
12. W. W. Chow and F. Jahnke, "On the physics of semiconductor quantum dots for applications in lasers and quantum optics," Prog. Quantum Electron. **37**, 109–184 (2013).
13. S. S. Mikhrin, A. R. Kovsh, I. L. Krestnikov, A. V. Kozhukhov, D. A. Livshits, N. N. Ledentsov, Y. M. Shernyakov, I. I. Novikov, M. V. Maximov, and V. M. Ustinov, "High power temperature-insensitive 1.3 μm InAs/InGaAs/GaAs quantum dot lasers," Semicond. Sci. Technol. **20**, 340–342 (2005).
14. J. K. Mee, M. T. Crowley, N. Patel, D. Murrell, R. Raghunathan, A. Aboketaf, A. Elshaari, S. F. Preble, P. Ampadu, and L. F. Lester, "A passively mode-locked quantum-dot laser operating over a broad temperature range," Appl. Phys. Lett. **101**, 071112 (2012).
15. S. Chen, W. Li, J. Wu, Q. Jiang, M. Tang, S. Shutts, S. N. Elliott, A. Sobiesierski, A. J. Seeds, and I. Ross, "Electrically pumped continuous-wave III–V quantum dot lasers on silicon," Nat. Photonics **10**, 307–311 (2016).
16. Y. Shen, N. C. Harris, S. Skirlo, M. Prabhu, T. Baehr-Jones, M. Hochberg, X. Sun, S. Zhao, H. Larochelle, and D. Englund, "Deep learning with coherent nanophotonic circuits," Nat. Photonics **11**, 441–446 (2017).
17. D. Goulding, S. P. Hegarty, O. Rasskazov, S. Melnik, M. Hartnett, G. Greene, J. G. McInerney, D. Rachinskii, and G. Huyet, "Excitability in a quantum dot semiconductor laser with optical injection," Phys. Rev. Lett. **98**, 153903 (2007).
18. M. Dillane, J. Robertson, M. Peters, A. Hurtado, and B. Kelleher, "Neuromorphic dynamics with optically injected quantum dot lasers," Eur. Phys. J. B **92**, 197 (2019).
19. G. Sarantoglou, M. Skontranis, and C. Mesaritakis, "All optical integrate and fire neuromorphic node based on single section quantum dot laser," IEEE J. Sel. Top. Quantum Electron. **26**, 1900310 (2020).
20. C. Mesaritakis, A. Kapsalis, A. Bogris, and D. Syvridis, "Artificial neuron based on integrated semiconductor quantum dot mode-locked lasers," Sci. Rep. **6**, 39317 (2016).
21. E. M. Izhikevich, *Dynamical Systems in Neuroscience* (MIT, 2007).
22. R. FitzHugh, "Mathematical models of threshold phenomena in the nerve membrane," Bull. Math. Biophys. **17**, 257–278 (1955).
23. M. Krupa and P. Szmolyan, "Relaxation oscillation and canard explosion," J. Differ. Equ. **174**, 312–368 (2001).
24. F. Marino, G. Catalán, P. Sánchez, S. Balle, and O. Piro, "Thermo-optical 'canard orbits' and excitable limit cycles," Phys. Rev. Lett. **92**, 073901 (2004).
25. E. M. Izhikevich, "Resonate-and-fire neurons," Neural Netw. **14**, 883–894 (2001).
26. A. Dolcemascolo, B. Garbin, B. Peyce, R. Veltz, and S. Barland, "Resonator neuron and triggering multipulse excitability in laser with injected signal," Phys. Rev. E **98**, 062211 (2018).
27. C. Mesaritakis, M. Skontranis, G. Sarantoglou, and A. Bogris, "Micro-ring-resonator based passive photonic spike-time-dependent-plasticity scheme for unsupervised learning in optical neural networks," in *Optical Fiber Communications Conference and Exhibition (OFC)* (IEEE, 2020), pp. 1–3.
28. S. Thorpe, A. Delorme, and R. Van Rullen, "Spike-based strategies for rapid processing," Neural Netw. **14**, 715–725 (2001).

29. J. L. Dubbeldam and B. Krauskopf, "Self-pulsations of lasers with saturable absorber: dynamics and bifurcations," Opt. Commun. **159**, 325–338 (1999).
30. J. L. Dubbeldam, B. Krauskopf, and D. Lenstra, "Excitability and coherence resonance in lasers with saturable absorber," Phys. Rev. E **60**, 6580–6588 (1999).
31. A. Röhm, *Dynamic Scenarios in Two-State Quantum Dot Lasers: Excited State Lasing, Ground State Quenching, and Dual-Mode Operation* (Springer, 2015).
32. M. Ishida, N. Hatori, T. Akiyama, K. Otsubo, Y. Nakata, H. Ebe, M. Sugawara, and Y. Arakawa, "Photon lifetime dependence of modulation efficiency and *K* factor in 1.3 μm self-assembled InAs/GaAs quantum-dot lasers: impact of capture time and maximum modal gain on modulation bandwidth," Appl. Phys. Lett. **85**, 4145–4147 (2004).
33. C. Mesaritakis, C. Simos, H. Simos, A. Kapsalis, E. Roditi, I. Krestnikov, and D. Syvridis, "Effect of the number of quantum dot layers and dual state emission on the performance of InAs/InGaAs passively mode-locked lasers," Appl. Phys. Lett. **101**, 251115 (2012).
34. M. Gioannini, "Ground-state power quenching in two-state lasing quantum dot lasers," J. Appl. Phys. **111**, 043108 (2012).
35. C. Mesaritakis, C. Simos, H. Simos, I. Krestnikov, and D. Syvridis, "Dual ground-state pulse generation from a passively mode-locked InAs/InGaAs quantum dot laser," Appl. Phys. Lett. **99**, 141109 (2011).
36. M. Sugawara, N. Hatori, H. Ebe, M. Ishida, Y. Arakawa, T. Akiyama, K. Otsubo, and Y. Nakata, "Modeling room-temperature lasing spectra of 1.3-μm self-assembled InAs/GaAs quantum-dot lasers: homogeneous broadening of optical gain under current injection," J. Appl. Phys. **97**, 043523 (2005).
37. A. Tierno, N. Radwell, and T. Ackemann, "Low-frequency self-pulsing in single-section quantum-dot laser diodes and its relation to optothermal pulsations," Phys. Rev. A **84**, 043828 (2011).
38. E. A. Viktorov, T. Erneux, B. Tykalewicz, D. Goulding, S. P. Hegarty, G. Huyet, and B. Kelleher, "Optothermal excitabilities and instabilities in quantum dot lasers," Proc. SPIE **9357**, 935704 (2015).
39. E. A. Viktorov and T. Erneux, "Self-sustained pulsations in a quantum-dot laser," Phys. Rev. E **90**, 052914 (2014).
40. E. A. Viktorov, M. A. Cataluna, L. O'Faolain, T. F. Krauss, W. Sibbett, E. U. Rafailov, and P. Mandel, "Dynamics of a two-state quantum dot laser with saturable absorber," Appl. Phys. Lett. **90**, 121113 (2007).
41. S. H. Strogatz, *Nonlinear Dynamics and Chaos with Student Solutions Manual: With Applications to Physics, Biology, Chemistry, and Engineering* (CRC Press, 2018).
42. T. Erneux and P. Glorieux, *Laser Dynamics* (Cambridge University, 2010).
43. A. G. Vladimirov, U. Bandelow, G. Fiol, D. Arsenijević, M. Kleinert, D. Bimberg, A. Pimenov, and D. Rachinskii, "Dynamical regimes in a monolithic passively mode-locked quantum dot laser," J. Opt. Soc. Am. B **27**, 2102–2109 (2010).
44. D. B. Malins, A. Gomez-Iglesias, S. J. White, W. Sibbett, A. Miller, and E. U. Rafailov, "Ultrafast electroabsorption dynamics in an InAs quantum dot saturable absorber at 1.3 μm," Appl. Phys. Lett. **89**, 171111 (2006).
45. G. Kozyreff and T. Erneux, "Singular Hopf bifurcation to strongly pulsating oscillations in lasers containing a saturable absorber," Eur. J. Appl. Math. **14**, 407–420 (2003).
46. S. Breuer, M. Rossetti, L. Drzewietzki, P. Bardella, I. Montrosset, and W. Elsasser, "Joint experimental and theoretical investigations of two-state mode locking in a strongly chirped reverse-biased monolithic quantum dot laser," IEEE J. Quantum Electron. **47**, 1320–1329 (2011).
47. C. Mesaritakis, C. Simos, H. Simos, A. Kapsalis, I. Krestnikov, and D. Syvridis, "External optical feedback-induced wavelength selection and *Q*-switching elimination in an InAs/InGaAs passively mode-locked quantum dot laser," J. Opt. Soc. Am. B **29**, 1071–1077 (2012).
48. G. Sarantoglou, M. Skontranis, A. Bogris, and C. Mesaritakis, "Temporal resolution enhancement in quantum-dot laser neurons due to ground state quenching effects," in *Optical Fiber Communication Conference* (Optical Society of America, 2020), paper M2K-1.
49. G. J. Spühler, R. Paschotta, R. Fluck, B. Braun, M. Moser, G. Zhang, E. Gini, and U. Keller, "Experimentally confirmed design guidelines for passively *Q*-switched microchip lasers using semiconductor saturable absorbers," J. Opt. Soc. Am. B **16**, 376–388 (1999).
50. D. G. Deppe, K. Shavritranuruk, G. Ozgur, H. Chen, and S. Freisem, "Quantum dot laser diode with low threshold and low internal loss," Electron. Lett. **45**, 54–56 (2009).
51. O. Qasaimeh, W.-D. Zhou, J. Phillips, S. Krishna, P. Bhattacharya, and M. Dutta, "Bistability and self-pulsation in quantum-dot lasers with intracavity quantum-dot saturable absorbers," Appl. Phys. Lett. **74**, 1654–1656 (1999).